Hindawi Publishing Corporation
International Journal of Photoenergy
Volume 2016, Article ID 2953592, 11 pages
http://dx.doi.org/10.1155/2016/2953592

Research Article

Effect of Codoping Cl Anion and 5-AVA Cation on Performance of Large-Area Perovskite Solar Cells with Double-Mesoporous Layers

Yaxian Pei, Xiaoping Zou, Yingxiang Guan, and Gongqing Teng

Research Center for Sensor Technology, Beijing Key Laboratory for Sensor, Ministry of Education Key Laboratory for Modern Measurement and Control Technology, School of Applied Sciences, Beijing Information Science and Technology University, Jianxiangqiao Campus, Beijing 100101, China

Correspondence should be addressed to Xiaoping Zou; xpzou2014@163.com

Received 27 May 2016; Revised 20 July 2016; Accepted 2 August 2016

Academic Editor: Hongxia Wang

For the perovskite solar cells (PSCs), the performance of the PSCs has become the focus of the research by improving the quality of the perovskite absorption layer. So far, the performance of the large-area PSCs is lower than that of small-area PSCs. In the paper, the experiments were designed to improve the photovoltaic performance of the large-area PSCs by improved processing technique. Here we investigated the optoelectronic properties of the prototypical $CH_3NH_3PbI_3$ ($MAPbI_3$) further modulated by introducing other extrinsic ions (specifically codoped Cl^- and 5-AVA^+). Moreover, we used inorganic electron extraction layer to achieve very rapid photogenerated carrier extraction eliminating local structural defects over large areas. Ultimately, we fabricated a best-performing perovskite solar cell based on codoping Cl anion and 5-AVA cation which uses a double layer of mesoporous TiO_2 and ZrO_2 as a scaffold infiltrated with perovskite and does not require a hole-conducting layer. The experiment results indicated that an average efficiency of double-mesoporous layer-based devices with codoping Cl anion and 5-AVA cation was obtained with exceeding 50% enhancement, compared to that of pure single-mesoporous layer-based device.

1. Introduction

Organic–inorganic metal halide perovskite solar cells, particularly the $MAPbX_3$ (where MA denotes methylammonium cations and X = I, Cl, and Br) perovskite as a light harvesting material, have recently attracted tremendous attention due to their low cost and outstanding desirable properties [1]. Currently, continuous efforts will be focused on the investigation of the high efficiency and stability of the $CH_3NH_3PbX_3$ PSCs with electron or hole transport layer. However, employing perovskites with mixed cations and halides has also become significant because the pure perovskite compounds suitable for photovoltaic applications, which are mainly $MAPbX_3$, $FAPbX_3$ (where FA denotes formamidinium cations), and $CsPbX_3$ (where Cs refers to inorganic cesium), possess numerous disadvantages. Cl incorporation into the perovskite crystal structure was initially investigated by Colella et al. [2]. They found that the Cl doping dramatically improves the charge transport within the perovskite layer. Moreover, it was reported that adding $PbCl_2$ to the precursor solution could influence the morphology of perovskite, resulting in an increase of the power conversion efficiency (PCE) [3–5]. In 2015, Chen et al. found that the chlorine incorporation mainly improved the carrier transport across the heterojunction interfaces, rather than within the perovskite crystals, leading to a PCE of 17.91% [6]. In addition, Suzuki and coworkers investigated the role of halogen doping using iodine, bromine, and chlorine compounds as dopant on the photovoltaic performance and microstructures of $CH_3NH_3PbI_{3-x-y}Br_xCl_y$ perovskite solar cells [7]. Materials property evolution has been recorded when replacing lead with tin, where the absorption edge can be successfully red-shifted to over 1000 nm in $CH_3NH_3Sn_xPb_{(1-x)}I_3$ perovskites [8]. Regarding the site of MA cation, 5-AVA replaced part of the MA cations in the cuboctahedral site of $MAPbI_3$, forming the mixed cation $(5\text{-AVA})_x(MA)_{1-x}PbI_3$ perovskite reported

by Mei et al. [9]. The $FA_{1-x}MA_xPb(I_{1-y}Br_y)_3$ perovskite was prepared to further improve the performance of perovskite based photovoltaics [10]. In addition, the group of McMeekin fabricated PSCs that reached open-circuit voltages of 1.2 volts and power conversion efficiency of over 17% on small area [11]. Bi et al. also produced the perovskite films in a single step from a solution containing a mixture of FAI, PbI_2, MABr, and $PbBr_2$ [12]. To date, Saliba et al. presented the notion that the use of all three cations (MA, FA, and Cs) offers additional versatility in tuning high quality perovskite films. The final result shows that the combination of different cations can combine the merits of the components while avoiding their flaws [13]. In addition, a double layer of mesoporous TiO_2 and ZrO_2 as a scaffold infiltrated with perovskite was used [9]. Liu et al. fabricated solar cells based on TiO_2/ZrO_2/carbon films with efficiency exceeding 13% [14].

Currently, PSCs typically require an expensive and air-sensitive hole transporter (e.g., spiro-MeOTAD) and a noble metal electrode (Au or Ag). To tackle high manufacturing cost, Ku and coworkers proposed for the first time that carbon black/graphite can substitute noble metallic materials as an efficient counter electrode in the application of hole-conductor-free $CH_3NH_3PbI_3$ perovskite/TiO_2 heterojunction solar cells [15]. Wei et al. employed abundant candle soot as an efficient hole extractor and reported a new strategy of clamping solar cells by judiciously interfacing the candle soot with $CH_3NH_3PbI_3$ films [16]. Subsequently, a planar perovskite solar cell that incorporates a nanocarbon hole-extraction layer is fabricated for the first time by an inkjet printing technique with a precisely controlled pattern and interface [17]. Among the various perovskite solar cells, the carbon-based hole-transporter-free type is the most promising for applications, owing to its low materials and manufacturing cost, high efficiency, and best long-term stability. However, the fill factor is typically below 0.75, limiting the cell performance. Therefore, Wei et al. highlighted two outstanding advantages for multiwall-carbon-nanotube-based devices: high FF and hysteresis-free performance [18]. Thus far, for carbon-based HTM-free PSCs, the highest power conversion efficiency of 14.38% is obtained, which is a record value [19]. In addition, Chan et al. proposed that the carbon layer as a p-type electrode was fabricated by screen-printing the carbon paste, which was prepared by mixing graphite, carbon black, Al_2O_3, ethyl cellulose, and alpha-terpineol [20]. Here, we adopted facile method and low-cost screen-printing carbon paste to fabricate the carbon layer as a back electrode.

Although numerous efforts have been concentrated on the investigation of small-area PSCs, the investigation of PSCs based on doping and without hole transport layer at an aperture area >1 cm^2 is insufficient. Chen et al. fabricated the large-area PSCs with an aperture area >1 cm^2 showing the highest PCE > 15% [21]. At present, utilizing films fabricated by vacuum-flash solution processing method, Li et al. demonstrated solar cells with an aperture area exceeding 1 cm^2 showing a maximum efficiency of 20.5% and a certified PCE of 19.6% [22].

Here we fabricate large-area PSCs with single-mesoporous layers using doping of the different elements to investigate the role of the extrinsic ion in the context of optoelectronic properties. The experiments indicate the performance of codoping perovskite is higher than that of single-doping perovskite. Furthermore, in order to compare with the performance of single-mesoporous-based PSCs with codoping, double-mesoporous-based PSCs with codoping are fabricated. Finally, an average efficiency of double-mesoporous layer-based devices with codoping Cl anion and 5-AVA cation was obtained with exceeding 50% enhancement, compared to that of pure single-mesoporous layer-based device.

2. Experiment and Methods

2.1. Materials. Unless stated otherwise, all materials were purchased from Sinopharm Chemical Reagent Beijing Co., Ltd., or Shanghai MaterWin New Materials Co., Ltd., and used as received. ZrO_2 printing paste was purchased from Wuhan National Laboratory for Optoelectronics. And carbon paste for screen-printing was purchased from Guangzhou Seaside Technology development Co., Ltd.

2.2. The Preparation of Perovskite Precursor Solution. The Cl anion was introduced into the perovskite lattice with a mixture of MAI and MACl in the precursor solution with the mole ratio of 4 : 1; that is, MAI: MACl precursor was prepared by mixing MAI and MACl in 2-propanol with the mole ratio (4 : 1) described elsewhere [23]. And the concentration of MA^+ in the precursor solution for doping Cl^- and undoping was kept at a 1 : 1 molar ratio. Li et al. [24] and Mei et al. [9] fabricated the $(5\text{-AVA})_x(MA)_{1-x}PbI_3$ precursor solution with a mixture of 5-AVAI and MAI of the mole ratio between 1 : 20 and 1 : 30. In the present work, the perovskite based on doping 5-AVA^+ precursor solution was fabricated in the same procedure, except that a mixture of MAI and $HOOC(CH_2)_4NH_3I$ (5-AVAI) with the mole ratio of 1 : 19 was used instead of MAI solution to introduce 5-AVA during the film growth. And the concentration of iodide anions in the precursor solution with/without doping 5-AVA^+ was maintained at a 1 : 1 molar ratio. The $(5\text{-AVA})_x(MA)_{1-x}PbI_{3-y}Cl_y$ precursor solution was prepared in the same procedure, except that a mixture of 5-AVAI, MACl, and MAI with the mole ratio of 1 : 4 : 15 was used. The total molar concentration is equal to the concentration of MAI (10 mg/mL).

2.3. Device Fabrication. The fluorine-doped tin oxide (FTO) conductive glasses were cleaned with detergent in an ultrasonic bath and rinsed with deionized water, followed by washing with the mixture of deionized water, ethanol, and acetone at 1 : 1 : 1 by volume, and they suffered from an ultraviolet treatment for one hour. The compact TiO_2 layer (cp-TiO_2) was spin-coated on the cleaned FTO conductive glasses at 2000 rpm for 60 s and annealed at 125°C for 5 min and then sintered at 500°C for 30 min.

In our trials, for the preparation of mesoporous layer, the following two steps were performed. (1) Single-mesoporous layer: TiO_2 paste was diluted by ethanol at 1 : 3.5 by weight and deposited on the FTO/cp-TiO_2 substrate by spin-coating method at 2000 rpm for 60 s and annealed at 125°C for 5 min and then sintered at 500°C for 30 min to form mesoporous TiO_2 (mp-TiO_2) layer. (2) Double-mesoporous layer: ZrO_2

paste was diluted by ethanol at 1 : 2 by weight and spin-coated on the FTO/cp-TiO_2/mp-TiO_2 substrate at 2000 rpm for 60 s and annealed at 125°C for 5 min, and then sintered at 500°C for 30 min.

The substrates were preheated at 70°C on a hot plate for 15 min. Then, the PbI_2 solution (1 mol/L) keept at 70°C was spin-coated on the top of mesoporous layer at 5500 rpm for 60 s, followed by thermal annealing at 100°C for 30 min. Then, MAI (dissolved in 2-propanol) and a mixture of MAI/MACl or MAI/5-AVAI or MAI/MACl/5-AVAI were spin-coated on top of the dried PbI_2 layer in a two-step program at 0 rpm and 5500 rpm for 30 s and 60 s, respectively. Then, the films were dried at 100°C for 30 min. Finally, a carbon counter electrode was screen-printed on the top of perovskite layer, employing carbon slurry diluted with cyclohexanone to 85 wt% and annealed at 120°C for 15 min. Then, the solar cells were hot-pressed at 120°C for 5 s and pressure was set to 0.2 MPa. The entire fabrication processes of PSCs were carried out under humidity of about 30% and outside the glove box. The active area is about $1.5 \pm 0.2\,cm^2$.

2.4. Characterization. The current density-voltage (*J-V*) curves were characterized with a VersaSTAT3 source meter under standard air-mass 1.5 global (AM1.5G) illumination ($100\,mW/cm^2$) provided by a solar simulator (Oriel Sol 3A). The scanning electron microscopy (SEM) images were performed with an S-4300 (CARL ZEISS, Germany) to observe the surface morphology of thin films. X-ray diffraction (XRD) was used to analyze the crystallinity and size of sample. The XRD measurement was obtained by Bruker D8 focus (Bruker Corporation, Germany). The analysis of element was detected by Energy Dispersive X-Ray Spectroscopy (EDS) (model SIGMA, CARL ZEISS, Germany). The ultraviolet-visible (UV-vis) absorption spectra were obtained by the test system, which consisted of AvaSpec-ULS2048XL, test software, AvaLight-DH-S-BAL as a light source, AvaSpere-50-REFL, AvaSphere-IRRAD, and so on. The monochromatic incident photon-to-electron (IPCE) was measured with an IPCE measurement system (Institute of Physics, CAS, China) in our laboratory.

3. Results and Discussions

3.1. Device Performance of PSCs Based on Doping Perovskite Layers. In this paper, we research the role of the different doping extrinsic ion (undoped, doped Cl^-, doped 5-AVA^+, and codoped Cl^- and 5-AVA^+) on the perovskite film layers. Device performance is characterized by current density-voltage (*J-V*) measurements under standard AM1.5G illumination ($100\,mW/cm^2$) under atmospheric condition, with statistical distribution shown in Figure 1 and the mean values on a batch of seven photovoltaic devices were illustrated in Table 1. As shown in Figure 1, reference devices, that is, without Cl incorporation (w/o), obtain short-circuit current density (J_{SC}) in the range of $3.62–5.14\,mA/cm^2$, open-circuit voltages (V_{OC}) in the range of 563–808 mV, and fill factors (FF) in the range of 28%–33%, resulting in the efficiency ranging from 0.61% to 1.31%. By comparison, better performance is observed for devices based on doping Cl^-: J_{SC} in the range of $3.53–4.9\,mA/cm^2$, V_{OC} in the range of 683–763 mV, and FF in the range of 33%–40%, yielding the PCE ranging from 0.93% to 1.43%. Compared with the reference devices, the devices based on doping 5-AVA^+ have the J_{SC} value of 4.05–$4.96\,mA/cm^2$, V_{OC} value of 656–761 mV, and FF value of 32%–38%, resulting in the PCE ranging from 0.92% to 1.42%. The best-performing PSCs for codoping Cl^- and 5-AVA^+ devices produce the J_{SC} value of $4.41–6.00\,mA/cm^2$, V_{OC} in the range of 661–767 mV, and FF in the range of 32%–41%, yielding the PCE ranging from 1.00% to 1.76%. As shown in Table 1, the average performance for devices based on doping Cl^- and codoping is superior to the devices based on no doping. The enhanced performance of devices using doping Cl^- and codoping in terms of J_{SC}, V_{OC}, and FF is possibly related to the reduction of both parasitic current loss and series resistance [6]. The results indicate that doping is beneficial to improving the performance of the PSCs.

Table 1: Experiment average photovoltaic parameters of single-mesoporous PSCs devices based on different doping.

Sample	Average			
	J_{SC} (mA/cm^2)	V_{OC} (mV)	FF (%)	η (%)
w/o	4.48	719	31	1.02
Doped Cl^-	4.53	733	37	1.24
Doped 5-AVA^+	4.46	711	36	1.14
Codoped	5.37	731	37	1.44

3.1.1. Effect of the Doped Cl^- on the Performance of the PSCs. The *J-V* curves for best-performing PSCs with/without Cl incorporation are shown in Figure 2. The doping Cl^- based perovskite devices show greatly improved performance, with J_{SC}, V_{OC}, and FF reaching values of $4.90\,mA/cm^2$, 763 mV, and 40%, respectively, corresponding to a PCE of 1.43%. However, the optimal PSCs without doping produced J_{SC} of $5.14\,mA/cm^2$, V_{OC} of 808 mV, and FF of 33%, yielding an efficiency of 1.31%. The reason may be that the Cl incorporation improves the carrier transport across the heterojunction interfaces, so as to suppress the recombination of interfaces, where consequently the efficiency is improved; that is, the devices with Cl incorporation present the reduction of both parasitic current loss and series resistance, which is in good accordance with the relatively high FF obtained for this device [6]. It is inferred that the improved average FF is associated with the Cl incorporation.

SEM measurement was conducted to characterize the morphological evolution of the perovskite films (Figures 3(a) and 3(b)). Compared with the w/o doped perovskite, it is noted that the perovskite size based on doping Cl^- becomes slightly larger. In order to gain insight into the effect of Cl incorporation, XRD analysis was performed to characterize the crystal structure of $MAPbI_3$ perovskites with Cl incorporation prepared on the FTO/cp-TiO_2/mp-TiO_2 substrates (Figure 4). As shown in Figure 4, the diffraction peak of perovskite based on doping Cl^- and w/o doping at 14.09° is assigned to the (110) lattice plane. As a comparison,

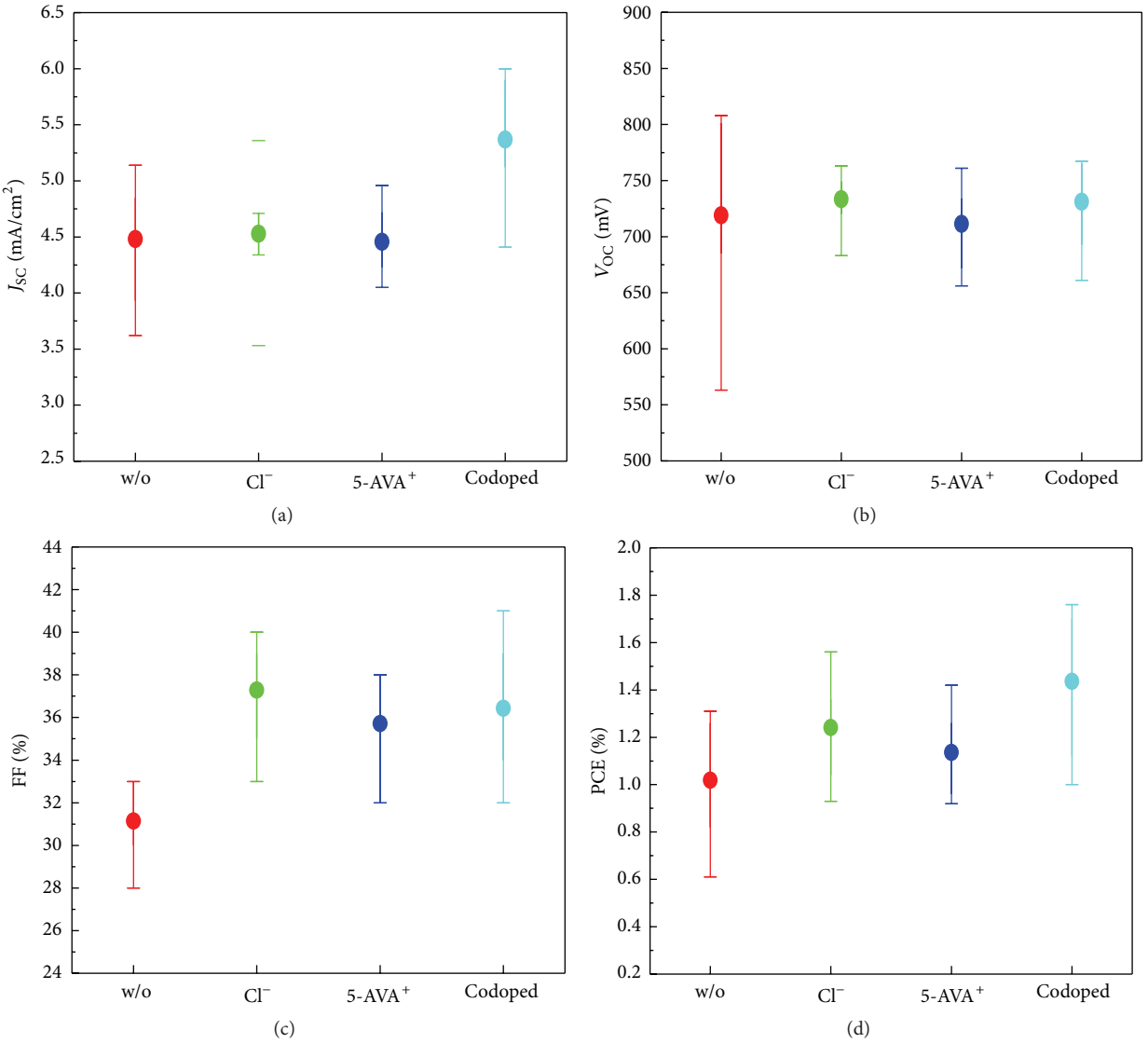

FIGURE 1: J-V characteristics of single-mesoporous PSCs with/without doping Cl^-, 5-AVA$^+$, and codoping: (a) the open-circuit voltage (V_{OC}), (b) short-circuit current density (J_{SC}), (c) fill factor (FF), and (d) power conversion efficiency (PCE).

it is found that the full width at half maximum (FWHM) of perovskite based on doping Cl^- with (110) diffraction peak becomes narrow; this indicates that the size of $MAPbI_3$ perovskite with doping Cl^- increases. This is in agreement with the analysis of SEM measurement. In addition, reducing the peak intensity of residual PbI_2 of the perovskite based on doping Cl^- is also observed. The result shows that the conversion of PbI_2 into the perovskite with doping Cl^- increases. EDS measurement is also performed to further analyze the Cl element incorporation into the perovskite lattice (Figure 3(c)). The combination of XRD and EDS indicates that the Cl element is introduced into the $MAPbI_3$ perovskite lattice.

In addition, both the UV-vis spectra and IPCE curves of the devices with/without doping Cl^- are presented in Figures 5(a) and 5(b). The corresponding integrated photocurrent calculated from the IPCE spectra with the AM1.5 solar emission are also shown in Figure 5(b). As shown in Figure 5(a), it is noted that the absorbance of the perovskite film with doping Cl^- is slightly higher than that of the devices without doping Cl^- in the range from 400 nm to 750 nm, which is consistent with the previous report [2]. The quantum efficiency in the IPCE of the PSCs based on doping Cl^- has a slight improvement, corresponding to the trend of UV-vis spectra.

3.1.2. Effect of the Doped 5-AVA$^+$ on the Performance of the PSCs. The J-V curves for best-performing PSCs with/without doping 5-AVA$^+$ are plotted in Figure 6. It is noted that the slope of the J-V curve at open-circuit voltage for $(5\text{-AVA})_x(MA)_{1-x}PbI_3$ perovskite is steeper than that of for $MAPbI_3$ perovskite, indicating a lower series resistance and higher electric conductivity for the former than for the latter

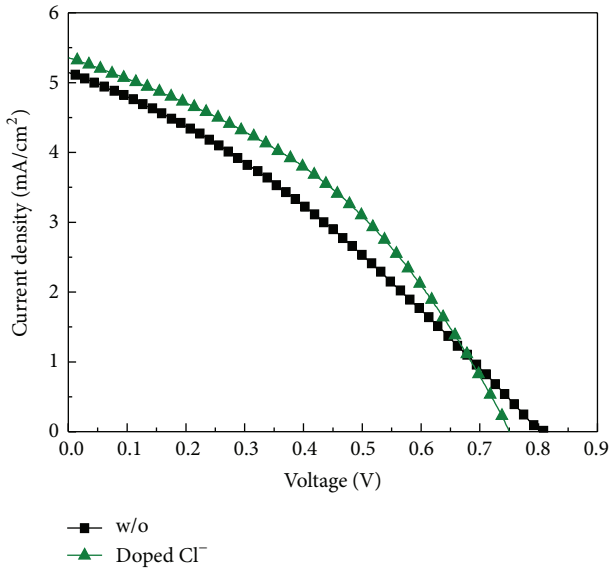

FIGURE 2: J-V characterization of the optimal PSCs with/without Cl incorporation.

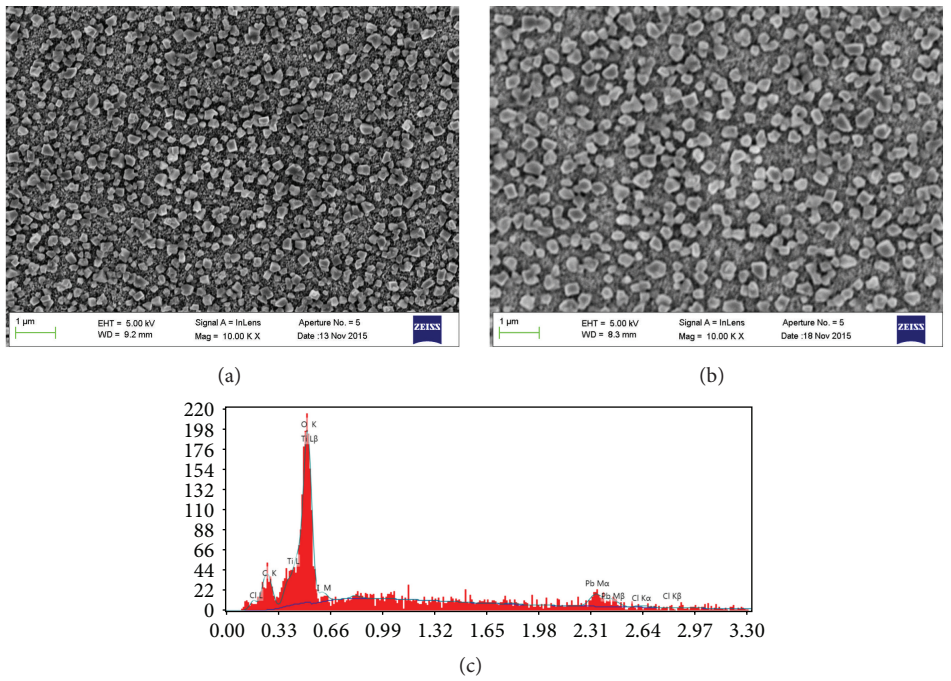

FIGURE 3: Top-view SEM images of the perovskite films without (a) and with (b) doping Cl$^-$. (c) EDS pattern of the perovskite based on doping Cl$^-$.

perovskite. Moreover, compared with the perovskite based on no doping, although the J_{SC} and V_{OC} of the device with doping 5-AVA$^+$ are lower, the efficiency is higher, which is related to the improvement of fill factor. The reason may be that the defect concentration of newly emerging (5-AVA)$_x$(MA)$_{1-x}$PbI$_3$ perovskite is lower than that of pure MAPbI$_3$ perovskite, leading to the reduction of internal recombination [9]. The XRD patterns of pure MAPbI$_3$ and (5-AVA)$_x$(MA)$_{1-x}$PbI$_3$ permeated into the mp-TiO$_2$ film are compared, as shown in Figure 7. It is found that the newly emerging diffraction peak arising from (111) lattice plane for (5-AVA)$_x$(MA)$_{1-x}$PbI$_3$ is stronger than the corresponding one for MAPbI$_3$. The results are in accordance with the previous report [9]. The 5-AVA substantially increases the b and c lattice parameters. The large expansion of the c axis induced by 5-AVA indicates its preferential alignment along this axis through contact with lead and iodide ions, and the c-axis becomes the dominant orientation during crystal growth [9].

The UV-vis spectra of pure MAPbI$_3$ and (5-AVA)$_x$(MA)$_{1-x}$PbI$_3$ perovskite are presented in Figure 8(a).

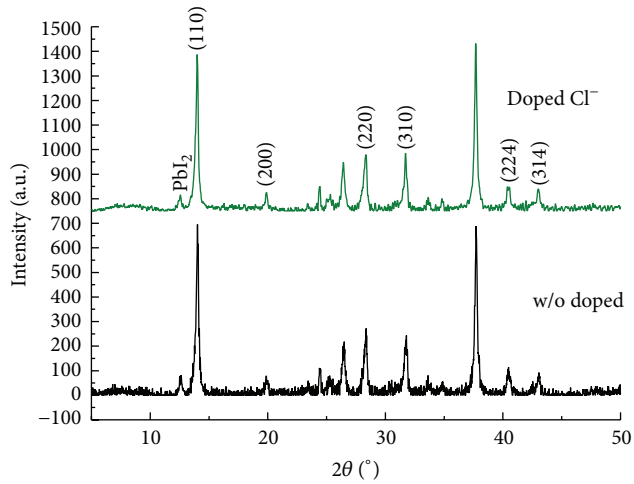

FIGURE 4: XRD patterns of perovskite films fabricated with different approaches (from top to bottom: doped Cl^- and w/o doped).

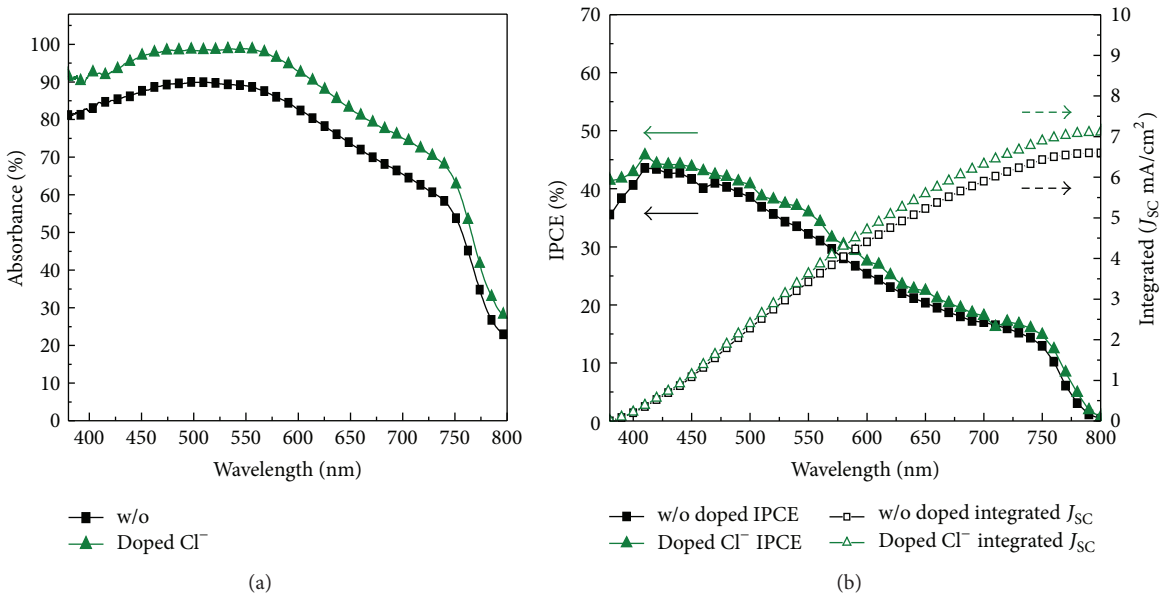

FIGURE 5: Perovskite film and device performance. (a) The UV-vis spectra of FTO glass/cp-TiO_2/mp-TiO_2 films filling with $MAPbI_3$ (black square) and $MAPbI_{3-y}Cl_y$ (olive triangle). (b) The IPCE curves and corresponding integrated photocurrent curves of the devices with/without doping Cl^-.

The absorption intensity of $(5\text{-AVA})_x(MA)_{1-x}PbI_3$ perovskite increases between 380 nm and 630 nm. Furthermore, the IPCE curves of the device with/without doping 5-AVA^+ are plotted in Figure 8(b). As shown in Figure 8(b), the change of external quantum efficiency is in keeping with that of UV-vis spectra. And the integrated photocurrent from IPCE measurement based on doping 5-AVA^+ is higher than that of the device without doping. The result is in agreement with the *J-V* measurement.

3.1.3. Effect of the Codoped Cl Anion and 5-AVA Cation on the Performance of the PSCs. The *J-V* curves measured at a simulated AM1.5 solar irradiation of 100 mW/cm^2 for the best-performing PSCs based on doping Cl^-, 5-AVA^+, and codoping are plotted in Figure 9(a). It is found that the photovoltaic performance of perovskite based on codoping is the best, indicating that the Cl^- and 5-AVA^+ coincorporation has a positive effect. The small addition of chloride ions to the pure $MAPbI_3$ results in such a remarkable increase in the electron-hole diffusion length, predominantly arising from substantial inhibition of nonradiative electron-hole recombination; that is, the larger diffusion length in the mixed halide perovskite results from a much longer recombination lifetime [25]. de Quilettes et al. have shown employing confocal fluorescence microscopy correlated with scanning electron microscopy [26] where the electron-hole recombination rate is strongly reduced in the presence of grain boundaries (GBs), while it is increased with Cl doping. This experiment clearly suggests that GBs are detrimental to perovskite solar cell performance due to accelerated electronic energy loss to heat.

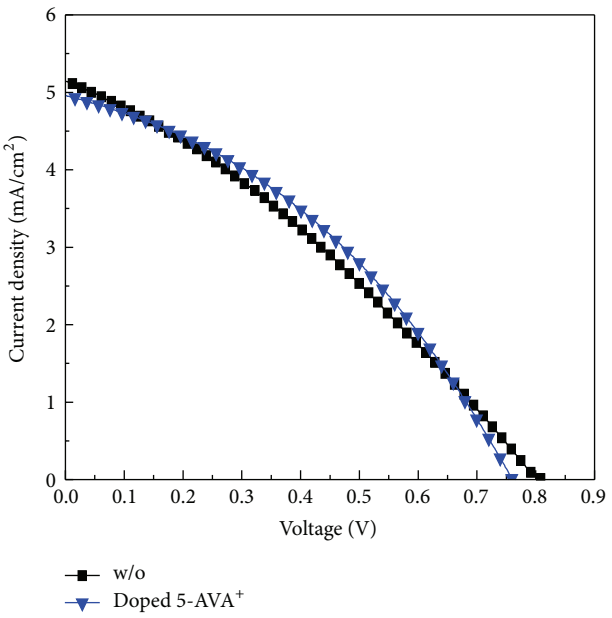

Figure 6: J-V characterization of the optimal PSCs with/without doping 5-AVA$^+$.

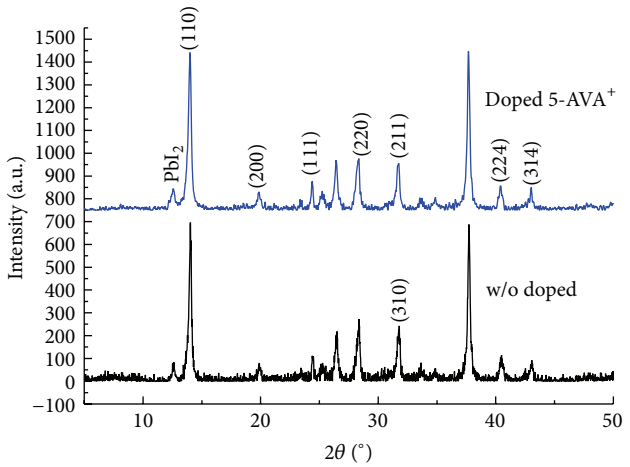

Figure 7: XRD patterns corresponding to perovskite films fabricated with/without doping 5-AVA$^+$.

To clarify the role of GBs and GB doping on the electron-hole recombination within $MAPbI_3$ perovskites, a real-time atomistic simulation is needed to mimic the electronic-vibrational dynamics directly as they occur in experiments. Long and coauthors presented the notion that GBs greatly accelerate the recombination, while introduction of substitutional Cl dopants at the boundary reduces the recombination, making it even slower than in the pristine $MAPbI_3$ [27]. It is found that the carrier transport across interface between perovskites and carrier transport layers is improved through the Cl incorporation, rather than within the perovskite film [6]. With regard to the influence of organic cation doping, Mercier [28] employed 4-ammonium-butyric acid (4-ABA) as a template for the engineering of $(4\text{-ABA})_2PbI_4$ and mixed-cation $(4\text{-ABA})_2MAPb_2I_7$ perovskite crystals. The ABA molecules formed linear hydrogen-bonded chains that serve as supramolecular synthons for layered plumbo iodide perovskite structures [28]. Mei et al. presented that the 5-AVA influences the crystal growth of $(5\text{-AVA})_x(MA)_{1-x}PbI_3$ in a similar fashion through the formation of hydrogen bonds between its COOH and NH_3^+ groups and I^- ions from the PbI_6 octahedra [9].

In order to explore the role of Cl and 5-AVA in perovskite film, the IPCE curves of the devices based on doping Cl^-, 5-AVA$^+$, and codoping are shown in Figure 9(b). Compared with the devices of doping Cl^- or 5-AVA$^+$, the external quantum efficiency of the devices based on codoping Cl^- and 5-AVA$^+$ is remarkably improved in the range of from 380 nm to 600 nm. The integrated photocurrent from IPCE measurement based on the codoping is higher than that of the devices based on single-doping. The results are in agreement with those of J-V measurements.

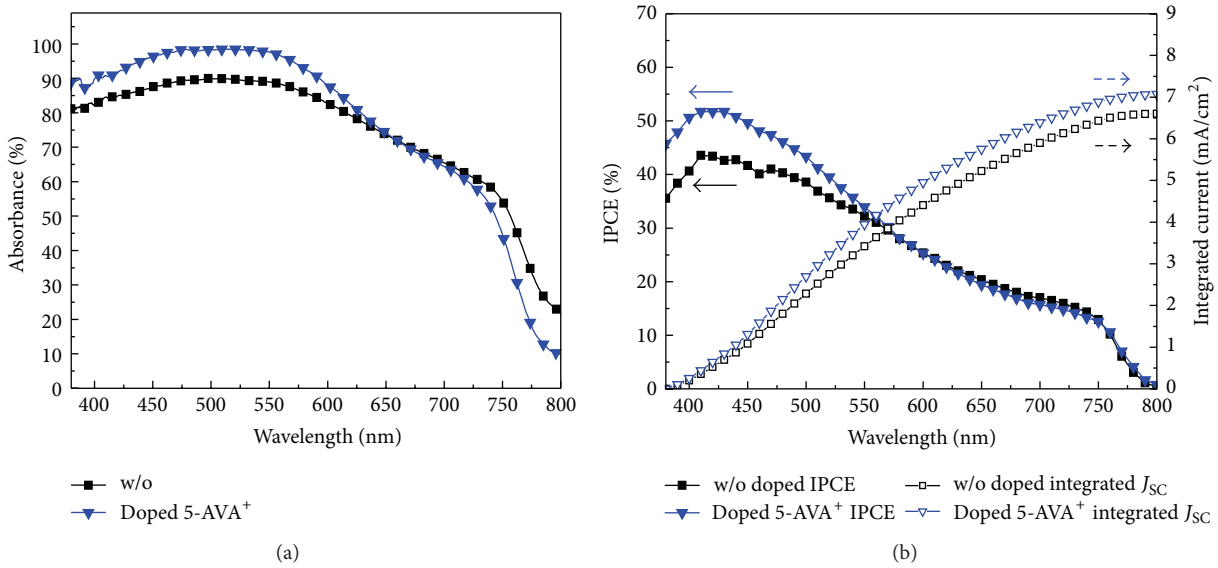

FIGURE 8: (a) The UV-vis spectra of FTO glass/cp-TiO_2/mp-TiO_2 films filling with $MAPbI_3$ (black) and $(5\text{-}AVA)_x(MA)_{1-x}PbI_3$ (blue). (b) The IPCE curves and corresponding integrated photocurrent curves of the devices with/without doping $5\text{-}AVA^+$.

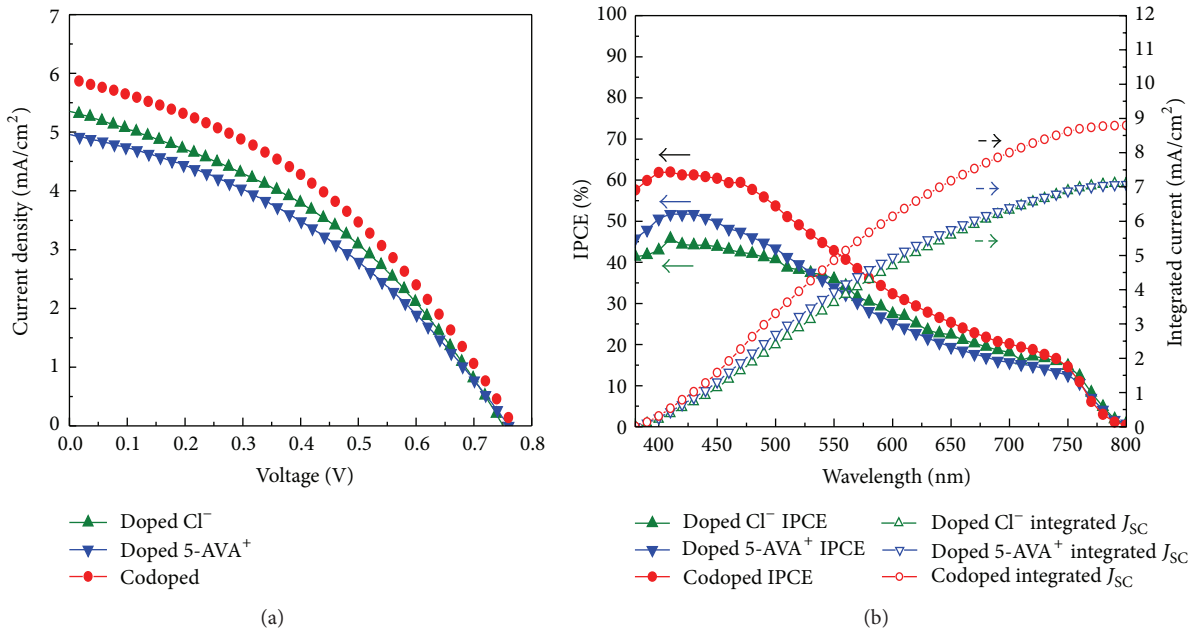

FIGURE 9: (a) *J-V* characterization of the optimal single-mesoporous-based PSCs with doping Cl^-, $5\text{-}AVA^+$, and codoping (Cl^- and $5\text{-}AVA^+$). (b) The IPCE curves and integrated photocurrent curves of the best-performing single-mesoporous-based devices with doping Cl^-, $5\text{-}AVA^+$, and codoping.

3.2. Device Performance of mp-TiO_2 and mp-TiO_2/mp-ZrO_2-Based PSCs with Codoping Cl Anion and 5-AVA Cation. The *J-V* curves of the $(5\text{-}AVA)_x(MA)_{(1-x)}PbI_{(3-y)}Cl_y$-based PSCs with porous TiO_2 and TiO_2/ZrO_2 scaffold under standard conditions (AM1.5 global solar light at 100 mW/cm^2 and room temperature) are shown in Figure 10. It is obvious that the photovoltaic performance of the $(5\text{-}AVA)_x(MA)_{(1-x)}PbI_{(3-y)}Cl_y$-based PSCs with TiO_2/ZrO_2 scaffold is markedly improved; that is, in the absence of ZrO_2, the photovoltaic performance of the mp-TiO_2-based PSCs with codoping Cl anion and 5-AVA cation is poor. This confirmed that the ZrO_2 is blocking the flow of photogenerated electrons to the back contact, preventing recombination with the holes from the perovskite at the back contact [8]. The IPCE curves for the $(5\text{-}AVA)_x(MA)_{(1-x)}PbI_{(3-y)}Cl_y$-based perovskite with porous TiO_2 and TiO_2/ZrO_2 scaffold and corresponding integrated photocurrent are presented in Figure 11. The higher IPCE of device with porous TiO_2/ZrO_2

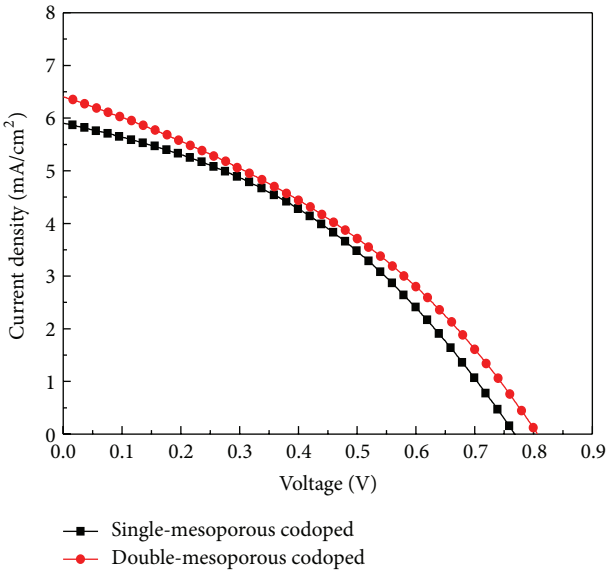

FIGURE 10: J-V characterization of the optimal (5-AVA)$_x$(MA)$_{(1-x)}$PbI$_{(3-y)}$Cl$_y$-based PSCs with single- and double-mesoporous layer.

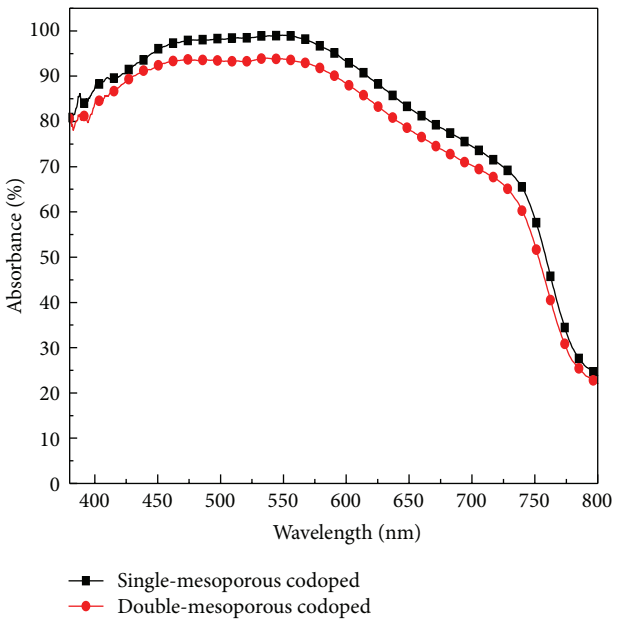

FIGURE 12: The UV-vis spectra of the device based on single- and double-mesoporous layer.

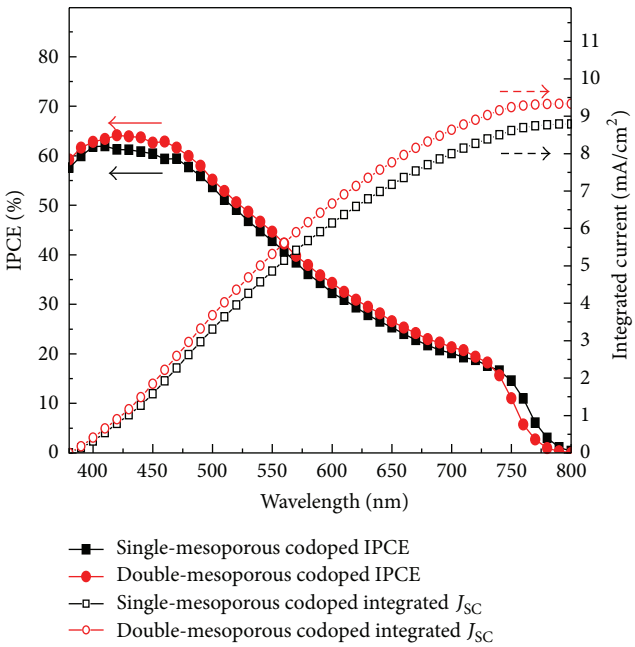

FIGURE 11: The IPCE curves and integrated photocurrent curves of the best-performing codoping-based PSCs with single- and double-mesoporous layer.

scaffold than device with porous TiO_2 is beneficial for higher loading amounts of (5-AVA)$_x$(MA)$_{(1-x)}$PbI$_{(3-y)}$Cl$_y$ perovskite [14]. And the integrated photocurrent calculated from IPCE measurement of the (5-AVA)$_x$(MA)$_{(1-x)}$PbI$_{(3-y)}$Cl$_y$-based perovskite based on double-mesoporous layer is higher than that of single-mesoporous layer. The result is consistent with that of J-V measurement. Furthermore, the UV-vis spectra of single-/double-mesoporous layer-based device with codoping Cl anion and 5-AVA cation are provided in Figure 12. As a comparison, the absorption intensity of the device based on double-mesoporous layer is lower than that of the device with single-mesoporous layer. This indicates that the light transmittance of the perovskite with double-mesoporous layer is weaker than that of single-mesoporous-based perovskite. The reason may be related to increasing the thickness of mesoporous layer, leading to increasing the internal recombination. However, the quantum efficiency in the IPCE of double-mesoporous-based device is higher than that of single-mesoporous-based device in the range of 380 nm to 550 nm. It is attributed to the insulation properties of ZrO_2 layer, resulting in avoiding the direct contact between carbon counter electrode and the cp-TiO_2 layer.

A hysteresis effect often occurs during measurement of the J-V curves of perovskite solar cells. The typical J-V characteristics of (5-AVA)$_x$(MA)$_{(1-x)}$PbI$_{(3-y)}$Cl$_y$ PSCs with single- and double-mesoporous layer at different scanning directions with a scan rate of 0.1 V/s are obtained under AM1.5 illumination (Figure 13). In terms of the scan direction, by comparison, no significant J-V hysteresis is observed in the device with double-mesoporous layer, which may be associated with increasing the thickness of mesoporous layer [29].

4. Conclusions

In summary, in our experiment, we investigated the role of the doping and single-/double-mesoporous layer in modifying the perovskite layers. We fabricated the best-performing

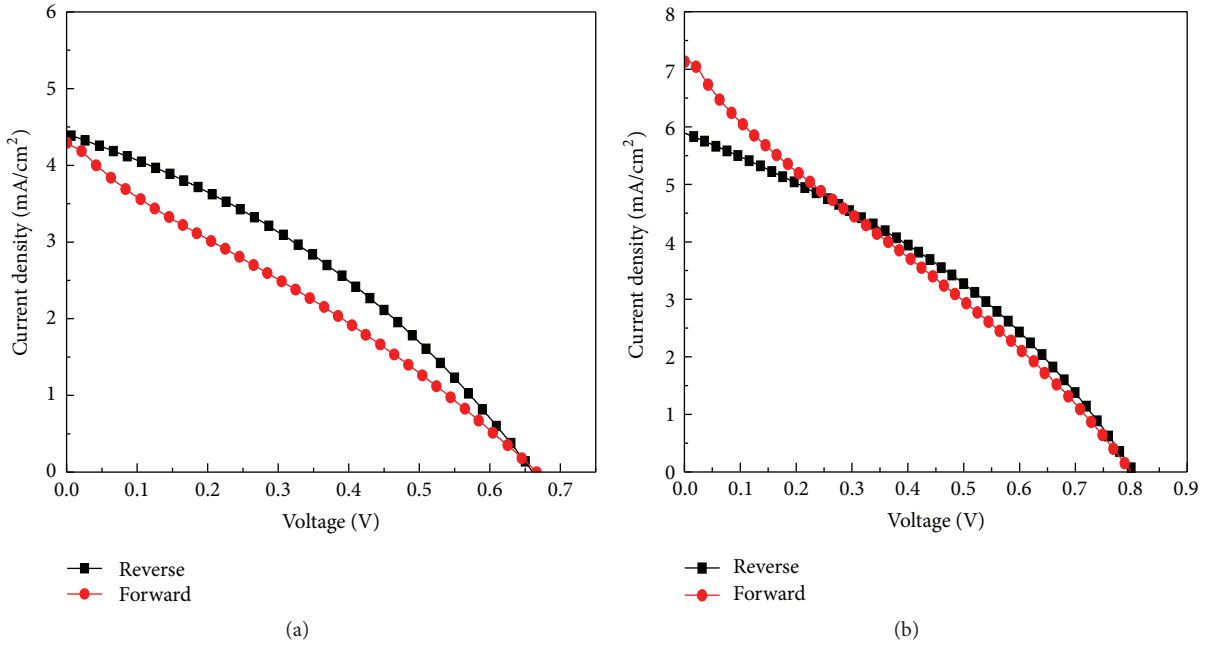

FIGURE 13: Hysteresis behavior of perovskite solar cells. The typical J-V characteristics of $(5\text{-AVA})_x(\text{MA})_{(1-x)}\text{PbI}_{(3-y)}\text{Cl}_y$-based PSCs with (a) single- and (b) double-mesoporous layer at different scanning directions: from short circuit to forward bias (black) and from forward bias to short circuit (red).

perovskite solar cell based on codoping Cl anion and 5-AVA cation which uses a double layer of mesoporous TiO_2 and ZrO_2 as a scaffold infiltrated with perovskite and does not require a hole-conducting layer. An average efficiency of double-mesoporous layer-based devices with codoping Cl anion and 5-AVA cation was obtained with exceeding 50% enhancement, compared to that of pure single-mesoporous layer-based $MAPbI_3$, due to the positive effect of codoping. Furthermore, the ZrO_2 with insulation property is blocking the flow of photogenerated electrons to the back contact, suppressing recombination with the holes from the perovskite at the back contact. In a word, the final experiment results are in agreement with the expectation, and it is confirmed that the performance of perovskite solar cell can be further improved by codoping. Continuous efforts will be concentrated on the investigation of charge transfer behaviors to further improve the device performance. For example, besides Cl and 5-AVA, other extrinsic ions for codoping can be incorporated into the perovskite solar cells by simply changing the reactants.

Competing Interests

The authors declare that there is no conflict of interests regarding the publication of this paper.

Acknowledgments

This work was partially supported by Project of Natural Science Foundation of China (91233201 and 61376057), Beijing Key Laboratory for Sensors of BISTU (KF20161077203), and Beijing Key Laboratory for Photoelectrical Measurement of BISTU (GDKF2013005).

References

[1] H.-S. Kim, S. H. Im, and N.-G. Park, "Organolead halide perovskite: new horizons in solar cell research," *Journal of Physical Chemistry C*, vol. 118, no. 11, pp. 5615–5625, 2014.

[2] S. Colella, E. Mosconi, P. Fedeli et al., "$MAPbI_{3-x}Cl_x$ mixed halide perovskite for hybrid solar cells: the role of chloride as dopant on the transport and structural properties," *Chemistry of Materials*, vol. 25, no. 22, pp. 4613–4618, 2013.

[3] Y. Ma, L. Zheng, Y.-H. Chung et al., "A highly efficient mesoscopic solar cell based on $CH_3NH_3PbI_{3-x}Cl_x$ fabricated via sequential solution deposition," *Chemical Communications*, vol. 50, no. 83, pp. 12458–12461, 2014.

[4] M. I. Dar, N. Arora, P. Gao, S. Ahmad, M. Grätzel, and M. K. Nazeeruddin, "Investigation regarding the role of chloride in organic-inorganic halide perovskites obtained from chloride containing precursors," *Nano Letters*, vol. 14, no. 12, pp. 6991–6996, 2014.

[5] E. Edri, S. Kirmayer, M. Kulbak, G. Hodes, and D. Cahen, "Chloride inclusion and hole transport material doping to improve methyl ammonium lead bromide perovskite-based high open-circuit voltage solar cells," *The Journal of Physical Chemistry Letters*, vol. 5, no. 3, pp. 429–433, 2014.

[6] Q. Chen, H. Zhou, Y. Fang et al., "The optoelectronic role of chlorine in $CH_3NH_3PbI_3(Cl)$-based perovskite solar cells," *Nature Communications*, vol. 5, no. 9, article 7269, 2015.

[7] A. Suzuki, H. Okada, and T. Oku, "Fabrication and characterization of $CH_3NH_3PbI_{3-x-y}Br_xCl_y$ perovskite solar cells," *Energies*, vol. 9, no. 5, p. 376, 2016.

[8] Y. Ogomi, A. Morita, S. Tsukamoto et al., "$CH_3NH_3Sn_xPb_{(1-x)}$ perovskite solar cells covering up to 1060 nm," *Journal of Physical Chemistry Letters*, vol. 5, no. 6, pp. 1004–1011, 2014.

[9] A. Mei, X. Li, L. Liu et al., "A hole-conductor-free, fully printable mesoscopic perovskite solar cell with high stability," *Science*, vol. 345, no. 6194, pp. 295–298, 2014.

[10] N. Pellet, P. Gao, G. Gregori et al., "Mixed-organic-cation perovskite photovoltaics for enhanced solar-light harvesting," *Angewandte Chemie—International Edition*, vol. 53, no. 12, pp. 3151–3157, 2014.

[11] D. P. McMeekin, G. Sadoughi, W. Rehman et al., "A mixed-cation lead mixed-halide perovskite absorber for tandem solar cells," *Science*, vol. 351, no. 6269, pp. 151–155, 2016.

[12] D. Bi, W. Tress, M. I. Dar et al., "Efficient luminescent solar cells based on tailored mixed-cation perovskites," *Science Advances*, vol. 2, no. 1, Article ID e1501170, 7 pages, 2016.

[13] M. Saliba, T. Matsui, J. Seo et al., "Cesium-containing triple cation perovskite solar cells: improved stability, reproducibility and high efficiency," *Energy & Environmental Science*, vol. 9, no. 6, pp. 1989–1997, 2016.

[14] T. Liu, L. Liu, M. Hu et al., "Critical parameters in TiO_2/ZrO_2/carbon-based mesoscopic perovskite solar cell," *Journal of Power Sources*, vol. 293, pp. 533–538, 2015.

[15] Z. Ku, Y. Rong, M. Xu, T. Liu, and H. Han, "Full printable processed mesoscopic $CH_3NH_3PbI_3$/TiO_2 heterojunction solar cells with carbon counter electrode," *Scientific Reports*, vol. 3, article 3132, 5 pages, 2013.

[16] Z. Wei, K. Yan, H. Chen et al., "Cost-efficient clamping solar cells using candle soot for hole extraction from ambipolar perovskites," *Energy & Environmental Science*, vol. 7, no. 10, pp. 3326–3333, 2014.

[17] Z. Wei, H. Chen, K. Yan, and S. Yang, "Inkjet printing and instant chemical transformation of a $CH_3NH_3PbI_3$/nanocarbon electrode and interface for planar perovskite solar cells," *Angewandte Chemie—International Edition*, vol. 53, no. 48, pp. 13239–13243, 2014.

[18] Z. Wei, H. Chen, K. Yan, X. Zheng, and S. Yang, "Hysteresis-free multi-walled carbon nanotube-based perovskite solar cells with a high fill factor," *Journal of Materials Chemistry A*, vol. 3, no. 48, pp. 24226–24231, 2015.

[19] H. Chen, Z. Wei, H. He, X. Zheng, K. S. Wong, and S. Yang, "Solvent engineering boosts the efficiency of paintable carbon-based perovskite solar cells to beyond 14%," *Advanced Energy Materials*, vol. 6, no. 8, Article ID 1502087, 2016.

[20] C. Chan, Y. Wang, G. Wu, and E. Wei-Guang Diau, "Solvent-extraction crystal growth for highly efficient carbon-based mesoscopic perovskite solar cells free of hole conductors," *J. Mater. Chem. A*, vol. 4, no. 10, pp. 3872–3878, 2016.

[21] W. Chen, Y. Wu, Y. Yue et al., "Efficient and stable large-area perovskite solar cells with inorganic charge extraction layers," *Science*, vol. 350, no. 6263, pp. 944–948, 2015.

[22] X. Li, D. Bi, C. Yi et al., "A vacuum flash-assisted solution process for high-efficiency large-area perovskite solar cells," *Science*, vol. 353, no. 6294, pp. 58–62, 2016.

[23] Q. Dong, Y. Yuan, Y. Shao, Y. Fang, Q. Wanga, and J. Huang, "Abnormal crystal growth in $CH_3NH_3PbI_{3-x}Cl_x$ using a multi-cycle solution coating process," *Energy Environmental Science*, vol. 8, no. 8, pp. 2464–2470, 2015.

[24] X. Li, M. Tschumi, H. Han et al., "Outdoor performance and stability under elevated temperatures and long-term light soaking of triple-layer mesoporous perovskite photovoltaics," *Energy Technology*, vol. 3, no. 6, pp. 551–555, 2015.

[25] S. D. Stranks, G. E. Eperon, G. Grancini et al., "Electron-hole diffusion lengths exceeding 1 micrometer in an organometal trihalide perovskite absorber," *Science*, vol. 342, no. 6156, pp. 341–344, 2013.

[26] D. W. de Quilettes, S. M. Vorpahl, S. D. Stranks et al., "Impact of microstructure on local carrier lifetime in perovskite solar cells," *Science*, vol. 348, no. 6235, pp. 683–686, 2015.

[27] R. Long, J. Liu, and O. V. Prezhdo, "Unravelling the effects of grain boundary and chemical dopingon electron-hole recombination in $CH_3NH_3PbI_3$ perovskite by time domain atomistic simulation," *Journal of the American Chemical Society*, vol. 138, no. 11, pp. 3884–3890, 2016.

[28] N. Mercier, "$(HO_2C(CH_2)_3NH_3)_2(CH_3NH_3)Pb_2I_7$: a predicted noncentrosymmetrical structure built up from carboxylic acid supramolecular synthons and bilayer perovskite sheets," *CrystEngComm*, vol. 7, no. 70, pp. 429–432, 2005.

[29] Y. Zhang, Z. Yao, S. Lin, J. Li, and H. Lin, "Perovskite solar cells: device construction and I-V hysteresis," *Acta Chimica Sinica*, vol. 73, no. 3, pp. 219–224, 2015.